Journal of Materials Chemistry A

Thermoelectric properties of $In_1Co_4Sb_{12+\delta}$: role of in situ formed InSb precipitates, Sb overstoichiometry, and processing conditions

Journal:	*Journal of Materials Chemistry A*
Manuscript ID	TA-ART-09-2022-007625.R1
Article Type:	Paper
Date Submitted by the Author:	21-Dec-2022
Complete List of Authors:	Ivanova, Alexandra; National University of Science and Technology MISIS Novitskii, Andrei; National University of Science and Technology MISIS, Academic Research Center for Energy Efficiency; NIMS Serhiienko, Illia; University of Tsukuba; NIMS Guélou, Gabin; NIMS Sviridova, Tatyana; National University of Science and Technology MISIS Novikov, Sergey; Ioffe Institute Gorshenkov, Mikhail; National University of Science and Technology MISIS Bogach, Alexey; Prokhorov General Physics Institute RAS Korotitskiy, Andrey; National University of Science and Technology MISIS Voronin, Andrei; National University of Science and Technology MISIS Burkov, Alexander ; Ioffe Institute Mori, Takao; NIMS; University of Tsukuba Khovaylo, Vladimir; National University of Science and Technology MISIS; National Research University Belgorod State University

ARTICLE

Thermoelectric properties of $In_1Co_4Sb_{12+\delta}$: role of *in situ* formed InSb precipitates, Sb overstoichiometry, and processing conditions§

Received 00th January 20xx,
Accepted 00th January 20xx

DOI: 10.1039/x0xx00000x

Alexandra Ivanova,[a,*,#] Andrei Novitskii,[a,b,#] Illia Serhiienko,[b,c,#] Gabin Guélou,[b,‡] Tatyana Sviridova,[a] Sergey Novikov,[d] Mikhail Gorshenkov,[a] Aleksei Bogach,[e] Andrey Korotitskiy,[a] Andrei Voronin,[a] Alexander Burkov,[d] Takao Mori[b,c] and Vladimir Khovaylo[a,f]

In-filled skutterudites $In_xCo_4Sb_{12}$ have attracted much attention due to their relatively high thermoelectric performance, which, in turn, is attributed to the In atoms acting as rattlers in the skutterudite voids and to the formation of InSb precipitates when the In solubility limit is exceeded ($0.22 \leqslant x_{max} \leqslant 0.27$). In this work, to suppress the formation of the unwanted $CoSb_2$ phase and favor the formation of the InSb precipitates, the following composition of $In_1Co_4Sb_{12+\delta}$ with In concentration much higher than the solubility limit and Sb overstoichiometry was used. Three sets of the bulk specimens with a nominal composition of $In_1Co_4Sb_{12+\delta}$ were synthesized by conventional induction melting followed by (1) ball milling (BM) and spark plasma sintering (SPS), (2) BM and SPS followed by high-temperature annealing, and (3) melt spinning and SPS. Utilization of different sample preparation methods and processing conditions leads to samples with different microstructure and InSb precipitates of different shape, size, and distribution. Thus, for all samples with the same nominal composition of $In_1Co_4Sb_{12+\delta}$, the zT_{max} varies from 0.7 to 1.3 at 673 K only because of microstructural modification. A maximum zT value of around 1.3 was obtained at 673 K for the sample prepared using induction melting followed by annealing, melt spinning, and SPS.

Introduction

Energy conversion and production are the foundation of modern civilization. However, the vast amount of produced energy is released in the form of so-called waste heat.[1] Therefore, in recent decades, considerable attention has been devoted to certain direct energy-conversion devices, notably thermoelectric (TE) generators, that bypass the intermediate step of conversion to mechanical energy in electrical power generation. TE devices, built from TE material legs, are solid-state systems able to utilize waste heat and directly convert it to electricity with no moving parts, being noise-free, low weight, low volume, and of special geometry for specific requirements. Despite all of these merits, the widespread application of TE systems is limited mainly due to their relatively low efficiency compared with other commercially available devices. The efficiency of TE devices is defined by temperature difference and the so-called dimensionless figure-of-merit, zT, of the material used as a working body. Here, $zT = \alpha^2\sigma T\kappa_{tot}^{-1}$, where α is the Seebeck coefficient, σ is the electrical conductivity, T is the absolute temperature, and κ_{tot} is the total thermal conductivity, including electronic, lattice, and bipolar contributions $\kappa_{tot} = \kappa_{el} + \kappa_{lat} + \kappa_{bip}$.[2] The effective TE material should exhibit a high power factor, $PF = \alpha^2\sigma$, and a low thermal conductivity in a wide temperature range. In other words, an ideal TE material should exhibit glass-like heat conduction of phonons and crystal-like electrical conduction of charge carriers referred to as the "phonon-glass electron-crystal" (PGEC) concept, first introduced by G. Slack in 1995.[3]

One of the most well-known and promising family of compounds representing the PGEC concept is $(Co,Fe)_4Sb_{12}$-based skutterudites. The key feature of the skutterudites is the presence of large voids in the crystal structure, into which a weakly bound guest atom can be placed.[4] Thus, while the covalently bonded framework provides high electrical conductivity, a guest species in the void serves as an effective scattering center for heat-carrying phonons through the

[a] National University of Science and Technology MISIS (NUST MISIS), Leninsky av. 4, Moscow, 119049, Russia.
[b] International Center for Materials Nanoarchitectonics (WPI-MANA), National Institute for Materials Science (NIMS), 1-1 Namiki, Ibaraki, Tsukuba, 305-0044, Japan.
[c] Graduate School of Pure and Applied Sciences, University of Tsukuba, 1-1-1 Tennodai, Ibaraki, Tsukuba, 305-8573, Japan.
[d] Ioffe Institute, Politekhnicheskaya st. 26, Saint Petersburg, 194021, Russia.
[e] Prokhorov General Physics Institute of the Russian Academy of Sciences, Vavilova st. 38, Moscow, 119991, Russia.
[f] Belgorod State University, Pobedy st. 85, Belgorod, 308015, Russia.
* Corresponding author. *E-mail address*: m154566@edu.misis.ru (A. Ivanova).
‡ Present address: CRISMAT, CNRS, Normandie University, ENSICAEN, UNICAEN, Caen, 14000, France.
# These authors contribute equally to the paper.
§ Electronic Supplementary Information (ESI) available: Scheme of the fabrication route for the samples under study; XRD data for all the samples before sintering; Rietveld refinements and its results; EBSD analysis data; SEM images of the fracture surfaces of the samples under study; SEM images of the polished surfaces with corresponding EDX mapping; field and angular dependencies of the Hall resistance; comparison of the thermoelectric properties of the MSA sample with those from previous reports; comparison of the charge carrier concentration and mobility of all the samples with those from literature. See DOI: 10.1039/x0xx00000x

localized vibrational modes (rattling effect). Furthermore, the guest species transfers electrons to the framework, which results in the additional enhancement of the power factor. Therefore, all of this provides a means of reduction of the lattice component of the thermal conductivity by order of magnitude without deleterious effects on the electrical transport parameters of the framework.

During the last decade, considerable progress has been achieved for both *p*- and *n*-type skutterudites. The most notable TE performance enhancement has been realized in multifilled skutterudites with elements of different mass and size at the rattler site (in the void) scattering phonons over a wide energy range and thus producing an even greater reduction in the thermal conductivity. Therefore, a zT above unity has been reported for many of the skutterudites.[4–8] Among various kinds of filled skutterudites, huge attention has been attracted to In-filled skutterudites where another additional mechanism of the lattice thermal conductivity reduction can be realized to achieve the $zT > 1$.[9–14] Initially, In atoms go into the filler site and the lattice thermal conductivity is greatly decreased along with the noticeable increase in the electrical conductivity.[9–14] However, when the solubility limit (maximum filling level in the cage of the framework) of In in $In_xCo_4Sb_{12}$ is exceeded ($0.16 \leqslant x_{max} \leqslant 0.27$),[9,11,12,15,16] the InSb secondary phase precipitates are formed predominantly at the grain boundaries of the main skutterudite phase.[10,13,14,16–18] This leads to an even more pronounced decrease in the lattice thermal conductivity and the electrical resistivity (so-called compositing effect).[19] Both the mechanisms account for excellent TE performance of the In-filled skutterudites and the zT of 1.4 – 1.5 at 700 K.[13,20] However, the formation of the InSb precipitates obviously leads to an Sb deficiency in the skutterudite phase and thus a formation of a $CoSb_2$ impurity phase, which usually results in the deterioration of the transport properties of the material.[9,10,16,21] Moreover, the Sb content itself plays an important role in the thermoelectric properties of Co_4Sb_{12} skutterudites.[22,23] Therefore Sb loss compensation is crucial in order to preserve a large amount of InSb precipitates along with the pure phase of the In-filled skutterudite matrix.[13,16] Besides the rattling effect, skutterudites exhibit a strong structure-properties relationship. Thus, the usage of different fabrication routes allows one to create a porous architecture,[14,24] a hierarchical structure,[25] or nanostructured bulks,[20,26] which also can contribute to the improvement of the transport properties of the skutterudites. Moreover, such processing techniques as ball milling or melt spinning, which are reported to be important for the lattice thermal conductivity reduction through the phonon scattering at grain boundaries, can also affect the distribution of the *in situ* formed precipitates of the secondary phase and thus the TE performance of the material.[27–29]

To reveal the unbiased influence of processing conditions, InSb precipitates and their distribution on the transport properties of the single filled skutterudites, we prepared three sets of the bulk specimens with a nominal composition of $In_1Co_4Sb_{12+\delta}$. The synthesis included induction melting (IM), as reported in our previous study,[13] followed by (1) ball milling or (2) melt spinning, and spark plasma sintering (SPS) followed by (3) high-temperature annealing (see Fig. S1). Due to the Sb overstoichiometry, it was possible to obtain samples with the lowest possible content of the $CoSb_2$ phase. At the same time, the use of different sample preparation methods and processing conditions made it possible not only to obtain samples with different microstructures but also with different distributions of InSb precipitates and/or porous architecture. In the samples obtained by melt spinning, InSb precipitates were found not only at the grain boundaries but also in the bodies of the grain, leading to a dramatic decrease in the thermal conductivity and a large zT value close to the best one reported for In-filled skutterudites.

Materials and methods

Induction melting. The ingot with a nominal composition of $In_1Co_4Sb_{12+\delta}$ was fabricated by the conventional induction melting technique from elemental In (99.9%, chunks), Co (99.95%, flakes), and Sb (99.9995%, chunks) as reported previously.[13] Raw materials were weighed according to the desired stoichiometry and melted in a Al_2O_3 crucible for 2 minutes followed by quenching in a cooper mold of cylindrical form. In order to compensate the Sb loss during the induction melting and the formation of InSb precipitates, ~10 wt.% excess of Sb was added to the composition before melting. The obtained ingot was cut into several parts and half of them were further annealed at 973 K for 5 h.

First set of the samples. Two of the ingots (one annealed and one not annealed) were ball milled using a Pulverisette 7 planetary micro mill (Fritsch, Germany) with stainless-steel balls (Ø 10 mm in diameter, powder-to-ball ratio of 1:5) and jars (volume of 45 ml) at 400 rpm for 60 min. The bulk samples were prepared from the obtained powders by a spark plasma sintering technique using a universal thermomechanical simulator Gleeble 3800 (Dynamic Systems Inc., USA). The powders were put into a cylindrical graphite die with a diameter of 10 mm, which was placed into the chamber and evacuated to a high vacuum. Uniaxial pressure was then applied through the top and bottom plungers. The samples were compressed at room temperature for 1 min, then the pressure was raised up to 50 MPa. Next, the temperature of the samples was gradually increased to 903 K with a heating rate of 50 K min^{-1}. After the holding time of 10 min, the pressure was reduced to 10 MPa, and the samples were freely cooled to room temperature. The compacted disc samples had dimensions of Ø 10 mm and ~12 mm height. After SPS, the specimens were annealed at 773 K for 10 h in an evacuated quartz tube. These two samples were labeled as BMAG and BMG (annealed after IM and not annealed after IM), respectively.

Second set of the samples. Another set of samples was prepared from the same powder (ball milled after IM). The samples were sintered using a Dr.Sinter-1080 SPS system (Fuji-SPS, Japan) with parameters exactly the same as those for the first set of samples. These two samples were annealed at 873 K for 5 h in an evacuated quartz tube and labeled as BMA and BM (annealed after IM and not annealed after IM), respectively. It should be noted that the annealing temperature was deliberately chosen to be higher than the melting temperature of the InSb phase in order to achieve the formation of a porous architecture, as shown in the previous work.[24]

Third set of the samples. Remained inductively melted ingots (again, one annealed and another one not annealed) were subjected to melt spinning (Melt Spinner MSP 10, Edmund Bühler GmbH, Germany). The ingots were placed into a quartz tube, melted, and injected under a pressure of 0.04 MPa high purity Ar onto a copper roller rotating at a linear speed of 30 – 40 m s^{-1}. The samples were sintered directly from the obtained ribbons using the same machine and parameters as those for the second set of samples. These two samples were additionally annealed after SPS at 773 K for 10 h in an

evacuated quartz tube and labeled as MSA and MS (annealed after IM and not annealed after IM), respectively. All the densified disk-shaped specimens of the second and the third sets had dimensions similar to those of the first set of the samples (see Fig. S1).

Characterization. Powder X-ray diffraction (PXRD) data were collected using a DRON-3 diffractometer (IC Bourevestnik, Russia) with CuK_α radiation (λ = 1.5417 Å). The Rietveld refinements against the PXRD patterns were carried out using the self-developed software package.[30] The relative error in the determination of the volume fractions of the phases was estimated to be within 5 – 10%, while the uncertainty in the lattice parameter was in the range of $0.0010 \leqslant \Delta a/a \leqslant 0.0015$. The morphology and chemical composition of the powders, ribbons, and bulk specimens were analyzed by scanning electron microscopy (SEM; Vega 3 SB, Tescan, Czech Republic) and energy dispersive X-ray spectroscopy (EDX; x-act, Oxford Instruments, UK). The accuracy of the EDX analysis is affected by many factors; the uncertainty of the obtained values of the constituents' actual content in the samples was estimated to be 10 – 15%. The microstructure details of the bulk samples were also supported by electron back scattered diffraction (EBSD) analysis with a step size of 400 nm by using a Vega 3 LMH SEM (Tescan, Czech Republic) equipped with NordLysMax^2 EBSD detector (Oxford Instruments, UK). EBSD data was processed using the open-source MTEX toolbox.[31] Transmission electron microscopy (TEM; JEM2100, JEOL, Japan) and EDX studies were performed using transparent foils prepared from the studied samples using conventional ion beam technique and bulks with polished surfaces. Consolidated pellets were cut into discs (Ø 10 × 1 mm^3) for the thermal diffusivity measurements and bars (10 × 3 × 1 mm^3) for the electrical transport properties measurements. The total thermal conductivity, κ, was calculated from the measured thermal diffusivity, χ, specific heat, C_p, and density d using the well-known relationship $\kappa = \chi C_p d$. The density of the samples was measured by the Archimedes principle. The specific heat C_p was calculated by the Debye model.[32] The thermal diffusivity was measured by the laser flash method using a HyperFlash LFA 467 (Netzsch, Germany) under continuous Ar flow. Lattice thermal conductivity, κ_{lat}, was obtained by subtracting the electronic contribution, κ_{el}, from the total thermal conductivity. The electronic thermal conductivity was estimated by the Wiedemann-Franz law: $\kappa_{el} = LT\sigma$, where L is the Lorenz number.[33] The Lorenz number was estimated as a function of temperature from the experimental values of the Seebeck coefficient in the framework of the effective mass model.[34] The electrical conductivity, σ, and the Seebeck coefficient, α, were measured simultaneously by a four-probe and differential methods, respectively, by a home-made measuring device in He atmosphere.[35] Moreover, the electrical transport properties were measured independently at the National University of Science and Technology MISIS (Moscow, Russia), Ioffe Institute (St. Petersburg, Russia), and National Institute for Materials Science (NIMS; Tsukuba, Japan). For the measurements of the electrical transport properties at NIMS, a commercial apparatus ZEM-2 (Ulvac-Riko, Japan) was used. The electrical transport properties were measured on heating and cooling, representing quite a reliable reproducibility. The Hall constant was measured at 290 K by two different techniques using a laboratory-made system (Cryotel, Russia). For both methods, five copper contacts and a current of 10 μA (3 μA for the BMG sample) were used. In the first case, the sample was aligned perpendicular to the magnetic field, H, and the resistivity, ρ, along with the Hall resistivity, ρ_H, were measured in a magnetic field range ±8 T. The Hall constant was determined from the slope of the obtained field dependence of the Hall resistivity ρ_H (H). Another approach was realized by the so-called stepwise rotation technique in a fixed magnetic field of 1 T. The Hall constant was calculated from the angular dependency of the Hall resistivity ρ_H (φ) with the magnetic field applied perpendicular to the rotation axis. ρ_H (φ) data were produced by the variation of the angle between the normal to the plane of the sample n and magnetic field H as a result of a change in the scalar product (n, H), which in turn modulates the Hall signal by harmonic simple sine law $\rho_H(\varphi) = \rho_{H0} + \rho_{H1}\sin(\varphi - \varphi_0)$, where ρ_{H0} is the constant bias term, and ρ_{H1} is the main component of the Hall signal. The amplitude of the harmonic term ρ_{H1} was used to calculate the Hall coefficient $R_H = \rho_{H1}/H$. The final value of the R_H was calculated as the average from both measurements by two methods. The Hall carrier concentration, n_H, and the Hall carrier mobility, μ_H, were calculated according to the following equations $n_H = 1/eR_H$ and $\mu_H = \sigma R_H$, respectively. The Hall measurement accuracy was within 5%. The uncertainty in the transport properties values is estimated to be within 8, 6, and 11% for the electrical conductivity, the Seebeck coefficient, and the total thermal conductivity, respectively. The combined uncertainty for all measurements involved in the zT calculation is 16%.[36]

Results and discussion

Compositional and structural characterizations. Powder X-ray diffraction analysis for all the samples was carried out during all the stages of the synthesis and displayed in the electronic supporting information file (ESI; Fig. S2). Right after induction melting, the ingot was mainly composed of Sb, $CoSb_2$, CoSb, InSb, and a small amount of $CoSb_3$ phase (Fig. S2a and Table S1). After the annealing, the In-filled skutterudite phase with InSb secondary phase was formed; however, a negligible trace of Sb phase still remained in the sample. The melt spinning of the as-cast ingot led to even more pronounced decomposition and, in fact, the formation of a $CoSb_2$-CoSb-Sb three-phase specimen (Fig. S2b). In turn, the melt spinning of the annealed ingot also led to the decomposition of the $CoSb_3$ phase to $CoSb_2$, CoSb, and Sb with a slightly higher amount of InSb and ~4 vol.% of $CoSb_3$ remaining in the sample (Fig. S2b and Table S1). This was quite expected from the In-Co-Sb phase diagram considering the rapid solidification during the melt spinning.[16] Thus, for all the samples except the BMAG and the BMA, the sintering stage can be considered as the so-called reactive SPS, where the $CoSb_3$ phase formation occurs along with the densification and grain growth processes. Here, we want to mention that there are many reports suggesting that SPS can be used not only as a densification step but also as a chemical reaction stage, which allows one to obtain the single phase material in a bulk form

from the prealloy or even raw materials.[37,38] Moreover, different microstructures can be expected for the samples subjected to the reactive SPS (usually, much smaller grain size) in comparison with those for the samples obtained by conventional SPS, as will be demonstrated later. All the samples after the sintering and annealing had a relatively high density and consisted mainly of the $CoSb_3$ skutterudite phase with traces of the InSb secondary phase (see Fig. 1 and Table 1). The unit cell parameter, *a*, was calculated by the Rietveld refinement of the PXRD patterns shown in Fig. 1 (see Fig. S3, Tables S2 and S3). For all the samples *a* is estimated to be 9.050(5) Å, which is in good agreement with previously reported data for In-filled skutterudites.[9,10,13,15] Moreover, this value of the unit cell parameter corresponds to the maximum filling fraction of indium at the 2*a* position in the unit cell, which is also confirmed by the EDX analysis (Table 1). As was mentioned before, the limit of indium incorporation into the voids of the $CoSb_3$ structure is about 0.22 – 0.27.[9,11,12,15,16] For all the samples this limit was reached, and thus the presence of the InSb phase was quite expected. It is worth noting that within the XRD detection limit, all the obtained samples do not contain the $CoSb_2$ phase, which usually deteriorates the electrical transport of the main phase and is formed due to the Sb deficiency in the skutterudite matrix attributed to the formation of InSb inclusions.[10,14,16,20,21] However, in our samples, the formation of the $CoSb_2$ phase was suppressed by the Sb overstoichiometry. Another point that we want to note is that there is a slightly higher content of indium in the skutterudite matrix in the MS and MSA samples. One possible reason for this is a slightly lower Co/Sb ratio of the MS series in comparison with that of the BM series, which determines the solubility limit of In in skutterudite according to the data on In-Co-Sb phase equilibria.[15,16] Another possible reason is that microstructure formed during the melt spinning (small grain size, a lot of subgrains) may accelerate, to some extent, diffusion of In inside the skutterudite phase.[20]

All samples exhibited different microstructures (Figs. S4, S5, Table S4), which is mainly attributed to the different processing conditions used to fabricate them. The BMG specimens showed a dense microstructure, void-free, and relatively uniform grain size (Figs. S4a, S5a) with an average grain size of 6 μm (Table 1). Moreover, the grains are much smaller in the BMG sample in comparison with those in the annealed after induction melting BMAG sample (Figs. S4b, S5b). Such a small grain size for the BM sample originated from the lack of annealing after induction melting and reactive sintering, during which the grains did not have enough time to grow. A similar microstructure was already reported for In-filled skutterudites obtained by long or high-energy ball milling followed by hot pressing.[7,20,39] The BMAG sample, in turn, has an average grain size of ~20 μm (Table 1) and inhomogeneous grain size distribution with small grains (< 1 μm) as well as big ones with sizes of 10 – 30 μm, which is also in line with results reported for skutterudites obtained by conventional techniques.[7,8] The microstructure and average grain size of the BM and BMA samples are similar to that of the BMG and BMAG, respectively. However, since high-temperature annealing was carried out right after the SPS, numerous pores and voids were observed for both samples (Figs. S5c, S5d). On the other hand, the microstructure of the MS series is rather different, with densely stacked shapeless grains of an average grain size of ~10 μm (Table 1) regardless of whether annealed or not annealed ingot was used for the fabrication (Figs. S5e, S5f, S4c, S4d). This was reasonably expected, considering that for the BM series, the difference in terms of the phase composition before sintering is striking, while for the MS series, in both cases, the phase composition before sintering is almost the same and represents a set of several phases (Fig. S2). However, what is more important is that the processing conditions affect not only the microstructure of the skutterudite but also the shape and distribution of the InSb inclusions, which play an important role in the electrical/thermal transport as will be discussed.

To evaluate and compare the distribution of the InSb precipitates in different samples, thorough SEM/EDX and TEM studies were carried out. It is important to note that the SEM images presented in Figure 2 were taken in the so-called electron channeling contrast mode,[40] which allows one to see grains of different orientations (similar to the EBSD analysis). In other words, the different grain colors in Figure 2 represent different orientations of the grains and not different phases as one would expect from SEM images in the conventional backscattered electrons (BSE) mode. Thus, such an analysis allowed us to establish that for the BMG sample, InSb inclusions envelop groups of closely stacked grains of the main skutterudite phase, as shown in Figure 2a (see also Figs. S4a, S6). At the same time, in the BMAG sample, the InSb phase envelops the grains of the main skutterudite phase, as was also observed in many previous studies on In-filled skutterudites (Figs. 2b, S4b, S7).[10,16,18] TEM analysis revealed that some indium was oxidized and, together with InSb precipitates, an insignificant amount of indium oxide In_2O_3 is located at the grain boundaries as well (Figs. 2c, S8a S8b). In all aspects relating to grain size, shape, and distribution of the InSb inclusions, the BM and the BMA samples follow those of the BMG and the BMAG specimens, respectively, with only one addition, which is a considerable number of pores (Figs. S9, S10). For the MS series, the distribution of the InSb inclusions is entirely different (Figs. 2d – f). First of all, it is important to note that the InSb phase does not envelop the grains but is located along their boundaries in the form of small dot-like inclusions (Figs. 2d, 2e). This may originate from a much higher solidification rate during the melt spinning compared to the induction melting.[18] Moreover, some of the dot inclusions are located not only at the grain boundaries but also in the body of the grains. From SEM and TEM observations, it seems that this is most likely a result of the grain boundaries migration during the sintering of the samples (see Figs. 2e, 2f). To the best of our knowledge, the formation of these dot-like inclusions at the grain boundaries as well as in the grain bodies is common for skutterudites fabricated by the melt spinning technique.[27,29] We also want to mention that the EDX analysis revealed that in all the samples except BMA/BMAG, a small amount of the $CoSb_2$ phase still remains (Figs. S6 – S12) despite the overstoichiometry of Sb,

but this amount is much lower than that observed in other studies.

All the discussed features of the microstructures of the samples will undoubtedly affect the electron and phonon transport mainly via the scattering of charge carriers and phonons at various scattering centers (grain boundaries, pores, inclusions, secondary phases, In rattling in the void), as will be discussed below.

Electrical transport. The electrical conductivity of all the samples exhibited the metal-like behavior over the whole temperature range measured as expected for heavily doped semiconductors (Fig. 3a). However, the absolute values of σ varied quite noticeably depending on the preparation route. Thus, the highest electrical conductivity at room temperature (1100 – 1200 $\Omega^{-1}cm^{-1}$) was achieved for the MS and the MSA samples, while the BMA and the BMAG samples exhibited lower values of around 1000 $\Omega^{-1}cm^{-1}$. In turn, the BMG and BM specimens demonstrated even lower values between 600 and 800 $\Omega^{-1}cm^{-1}$. Nevertheless, all these values are in a range from 600 to 1200 $\Omega^{-1}cm^{-1}$ that corresponds to the highest filling level of In in the void of the skutterudite (Fig. S13a). A closer inspection of the electrical transport properties was carried out considering the data for the Hall charge carrier mobility, μ_H, and concentration, n_H (Table 2). Magnetic field and angular dependencies of the Hall resistance are shown in Figs. S14, S15. One should keep in mind that $\sigma = en_H\mu_H$ (e is the electron charge), and thus, the difference in σ between the samples can be explained by taking into account several factors: (1) slightly different amount of In at the rattler position, as was mentioned previously, affects the charge carrier concentration since one In atom at void-filling position adds one extra electron to the system;[16,41] (2) different microstructures, in particular, grain size, results in different values of the μ_H since $\mu_H \propto L_g$, where L_g is the grain size; (3) size and distribution of the InSb precipitates also affects the electron transport through the scattering of charge carriers. Considering all of the above, the MS and the MSA samples with relatively big grains of ~10 μm, slightly higher amount of In in the matrix (Table 1), and nanoprecipitates at the grain boundaries and in their bodies (Figs. 2d, 2e, 2f), should exhibit higher n_H and more or less similar μ_H as was confirmed by the experiment (Table 2). In this context, it is apparent that the BMG (and the BM presumably) specimen exhibited the lower values of n_H, and μ_H (Table 2), and thus σ (Fig. 3a), due to its smaller grain size (Figs. 2a, S4a) and lower amount of In in the void (Table 1). n_H and μ_H achieved for all the samples in this work are similar to those reported for other In-filled skutterudites (Fig. S16).

Values of the Seebeck coefficient, α, exhibited an inverse trend, - that is, the samples with the highest σ values demonstrated the lowest α values (Fig. 3b). Along with this, all the samples exhibited negative Seebeck coefficient values throughout the whole temperature range, indicating n-type semiconductor behavior. Moreover, with increasing temperature, the absolute values of the Seebeck coefficient increased linearly for all the samples, as expected for degenerate semiconductors with $\alpha \propto Tn^{2/3}$ (T is the absolute temperature, and n is the charge carrier concentration).[42] However, at high temperatures ($T > 600$ K), the α leveled off and started to decrease, which is most likely attributed to the excitation of the minority charge carriers as was widely reported for $CoSb_3$-based thermoelectrics (see Fig. S13b).[7] This effect is more evident when analyzing the temperature dependence of the power factor, where the magnitude of $\alpha^2\sigma$ increased almost linearly with temperature and then started to decrease after reaching a peak (Fig. 3c). Overall, the samples prepared by the MS, MSA and BMA routes achieved the power factor of 35 – 40 μW cm^{-1} K^{-2} at 600 K, which is among the best values reported for In-filled skutterudites.[7,12,20]

Thermal transport. The overall thermal conductivity of all the samples ranged between 1.5 and 4 W m^{-1} K^{-1} and exhibited negative temperature dependence up to the temperature where the bipolar contribution starts playing a noticeable role (Fig. 4a). This is in line with the results for other In-filled skutterudites (Fig. S13c) and a few times lower than those for the pure Co_4Sb_{12}.[43] Such a significant decrease in the thermal conductivity is primarily attributed to the scattering of high-frequency phonons by indium atoms at the voids.[16] Besides, InSb precipitates play a significant role in the scattering of mid-to-long wavelength phonons, as reported previously.[13,44] In turn, the difference in the values of the thermal conductivity between the samples under study is likely arising from other scattering mechanisms associated with the microstructure (grain boundaries, pores) and hence the processing conditions. Thus, the lowest lattice thermal conductivity of 1.5 – 2 W m^{-1} K^{-1} at room temperature was achieved for the BM and the MSA samples (Fig. 4b). For the BM specimen, low κ_{lat} is mainly attributed to the small grain size and porous architecture formed during high-temperature annealing at 873 K (T_m(InSb) = 800 K). The formation of pores leads to an additional thermal conductivity reduction and can be roughly explained and estimated by the Eucken model.[45] For the MSA specimen the reason for low lattice thermal conductivity is different and most likely attributed to the different distribution, size, and shape of InSb precipitates located not only at the grain boundaries but in grain bodies as well (Fig. 2e). For all the samples the thermal conductivity increased at $T > 600$ K. Considering that both κ_{lat} and κ_{el} decreased with temperature, this growth at high temperatures is attributed to an increase of the bipolar conduction contribution to the total thermal conductivity as mentioned above. The common expression for bipolar thermal conductivity is $\kappa_{bip} = \sigma_h\sigma_e(\alpha_h - \alpha_e)^2T/\sigma$, where α_e and α_h are the Seebeck coefficients of electrons and holes, respectively, and σ is the sum of the electron conductivity, σ_e, and hole conductivity, σ_h.[46] Thus, to extract the bipolar thermal conductivity contribution, we plotted $\kappa_{lat} + \kappa_{bip}$ ($\kappa_{lat} + \kappa_{bip} = \kappa_{tot} - \kappa_{el} = \kappa_{tot} - \sigma LT$) and fitted lattice contribution by using power law $\kappa_{lat} \propto T^{-r}$ (solid lines in Fig. 4b). Accordingly, the bipolar thermal conductivity arose at $T > 600$ K when both holes and electrons are present and contributing to the electrical conductivity and the Seebeck coefficient (Fig. 3).

Thermoelectric figure of merit. For all samples with the same nominal composition of $In_1Co_4Sb_{12+\delta}$, the maximum value of zT varies from 0.7 to 1.3 at 673 K. This also can be demonstrated by the literature data for In-filled Co_4Sb_{12}, where compounds with more or less similar nominal chemical composition

exhibited zT in a range from 0.7 to 1.5 at 673 K (see Fig. S13d). Such a scatter of the values is primarily attributed to the microstructure (grain size, porosity), size, and distribution of InSb precipitates, which in turn is determined by the processing conditions. Thus, in this work, the highest zT_{max} of ~1.3 at 673 K was achieved for the MSA sample and a slightly lower zT_{max} was also obtained for the BM specimen at the same temperature. The attained $zT \approx 1.3$ is among the highest ever reported values for In-filled Co_4Sb_{12} skutterudites fabricated using different methods (Fig. S13d).

Conclusions

Three sets of samples were prepared using induction melting followed by various types of processing, including ball milling, melt spinning, SPS, and high-temperature annealing. PXRD and EDX analysis indicate that the maximum solubility limit of In in the voids of Co_4Sb_{12} was reached for all the samples. Moreover, it seems that specimens of the MS series had a slightly higher content of indium in the voids due to a lower Co/Sb ratio and/or accelerated diffusion of In inside the skutterudite phase during the melt spinning. In turn, the overstoichiometry of Sb led to a noticeable reduction of the $CoSb_2$ phase content (usually observed in such samples) along with the formation of InSb phase precipitates. It was also shown, that by using different processing conditions it is possible to obtain completely different microstructures. For instance, on the one hand, the absence of annealing after induction melting and technically speaking reactive SPS after it, allows one to obtain a fine-grained sample of the same chemical composition as in the case where the annealing stage is included. Annealing of such samples after SPS at a temperature above the melting point of the InSb precipitates resulted in the formation of a porous architecture, which leads to a substantial decrease in the thermal conductivity and, consequently, to an increase in the zT.[24] On the other hand, the use of melt spinning after induction melting resulted in a significant change in the size, shape, and distribution of InSb precipitates, which also affects both electrical and thermal transport. For all the samples mentioned above the thermoelectric properties were measured and a maximum zT value of around 1.3 was obtained at 673 K for the sample prepared using induction melting followed by annealing, melt spinning, and SPS. This value is close to the best reported results (see Fig. S13d).[13,20] This report can be useful for other researchers to improve other filled skutterudites through the modification of the microstructure (e.g., instead of complex multi-doping) by utilizing different processing conditions.

Author Contributions

Alexandra Ivanova: Methodology, Formal analysis, Investigation, Writing – original draft, Writing – Review & Editing. **Andrei Novitskii:** Conceptualization, Methodology, Data curation, Formal analysis, Investigation, Writing – original draft, Writing – Review & Editing, Visualization. **Illia Serhiienko:** Methodology, Investigation. **Gabin Guélou:** Investigation. **Tatyana Sviridova:** Investigation, Formal analysis. **Sergey Novikov:** Investigation. **Mikhail Gorshenkov:** Investigation, Formal analysis. **Aleksei Bogach:** Investigation. **Andrey Korotitskiy:** Investigation. **Andrei Voronin:** Conceptualization, Resources, Project administration, Funding acquisition. **Alexander Burkov:** Methodology, Resources, Writing – Review & Editing. **Takao Mori:** Resources, Writing – Review & Editing. **Vladimir Khovaylo:** Resources, Writing – Review & Editing, Supervision.

Conflicts of interest

There are no conflicts to declare.

Acknowledgements

The study was carried out with financial support from the Russian Science Foundation (project no. 19-79-10282). Takao Mori acknowledges JST Mirai JPMJMI19A1. A.N. and I.S. are very grateful to Dr. Dmitriy Karpenkov from the National University of Science and Technology MISIS for his encouraging philosophical discussions, invaluable advice, continuous support, and friendship.

Notes and references

1 D. D. Sarma, *ACS Energy Lett.*, 2021, **6**, 3715–3718.
2 A. F. Ioffe, *Semiconductor thermoelements, and Thermoelectric cooling*, Infosearch, London, 1957.
3 G. Slack, in *CRC Handbook of Thermoelectrics*, CRC Press, 1995.
4 G. Rogl and P. Rogl, *Curr. Opin. Green Sustain. Chem.*, 2017, **4**, 50–57.
5 G. Rogl, A. Grytsiv, P. Rogl, N. Peranio, E. Bauer, M. Zehetbauer and O. Eibl, *Acta Mater.*, 2014, **63**, 30–43.
6 G. Rogl, A. Grytsiv, P. Heinrich, E. Bauer, P. Kumar, N. Peranio, O. Eibl, J. Horky, M. Zehetbauer and P. Rogl, *Acta Mater.*, 2015, **91**, 227–238.
7 G. Rogl, A. Grytsiv, K. Yubuta, S. Puchegger, E. Bauer, C. Raju, R. C. Mallik and P. Rogl, *Acta Mater.*, 2015, **95**, 201–211.
8 G. Rogl, A. Grytsiv, P. Rogl, E. Bauer, M. B. Kerber, M. Zehetbauer and S. Puchegger, *Intermetallics*, 2010, **18**, 2435–2444.
9 T. He, J. Chen, H. D. Rosenfeld and M. A. Subramanian, *Chem. Mater.*, 2006, **18**, 759–762.
10 R. C. Mallik, C. Stiewe, G. Karpinski, R. Hassdorf and E. Müller, *J. Electron. Mater.*, 2009, **38**, 1337–1343.
11 J. Leszczynski, V. Da Ros, B. Lenoir, A. Dauscher, C. Candolfi, P. Masschelein, J. Hejtmanek, K. Kutorasinski, J. Tobola, R. I. Smith, C. Stiewe and E. Müller, *J. Phys. D. Appl. Phys.*, 2013, **46**, 495106.
12 E. Visnow, C. P. Heinrich, A. Schmitz, J. de Boor, P. Leidich, B. Klobes, R. P. Hermann, W. E. Müller and W. Tremel, *Inorg. Chem.*, 2015, **54**, 7818–7827.
13 V. V. Khovaylo, T. A. Korolkov, A. I. Voronin, M. V. Gorshenkov and A. T. Burkov, *J. Mater. Chem. A*, 2017, **5**, 3541–3546.
14 N. Gostkowska-Lekner, B. Trawinski, A. Kosonowski, B.

Bochentyn, M. Lapinski, T. Miruszewski, K. Wojciechowski and B. Kusz, *J. Mater. Sci.*, 2020, **55**, 13658–13674.

15 A. Grytsiv, P. Rogl, H. Michor, E. Bauer and G. Giester, *J. Electron. Mater.*, 2013, **42**, 2940–2952.

16 Y. Tang, Y. Qiu, L. Xi, X. Shi, W. Zhang, L. Chen, S.-M. Tseng, S. Chen and G. J. Snyder, *Energy Environ. Sci.*, 2014, **7**, 812–819.

17 H. Li, X. Tang, Q. Zhang and C. Uher, *Appl. Phys. Lett.*, 2009, **94**, 102114.

18 A. Sesselmann, T. Dasgupta, K. Kelm, E. Müller, S. Perlt and S. Zastrow, *J. Mater. Res.*, 2011, **26**, 1820–1826.

19 Z. Liu and T. Mori, in *System-Materials Nanoarchitectonics*, eds. Y. Wakayama and K. Ariga, Springer Tokyo, 1st edn., 2022, pp. 199–231.

20 M. Benyahia, V. Ohorodniichuk, E. Leroy, A. Dauscher, B. Lenoir and E. Alleno, *J. Alloys Compd.*, 2018, **735**, 1096–1104.

21 J. Leszczyński, W. Szczypka, C. Candolfi, A. Dauscher, B. Lenoir and A. Koleżyński, *J. Alloys Compd.*, 2017, **727**, 1178–1188.

22 W.-S. Liu, B.-P. Zhang, J.-F. Li and L.-D. Zhao, *J. Phys. D. Appl. Phys.*, 2007, **40**, 6784–6790.

23 Y. S. Lim, K.-H. Park, J. Y. Tak, S. Lee, W.-S. Seo, C.-H. Park, T. H. Kim, P. Park, I.-H. Kim and J. Yang, *J. Appl. Phys.*, 2016, **119**, 115104.

24 A. U. Khan, K. Kobayashi, D.-M. Tang, Y. Yamauchi, K. Hasegawa, M. Mitome, Y. Xue, B. Jiang, K. Tsuchiya, D. Golberg, Y. Bando and T. Mori, *Nano Energy*, 2017, **31**, 152–159.

25 J. Zhang, L. Zhang, W. Ren, W. Gou, J. Zhang and H. Geng, *ACS Appl. Mater. Interfaces*, 2021, acsami.1c06267.

26 M. S. Toprak, C. Stiewe, D. Platzek, S. Williams, L. Bertini, E. Müller, C. Gatti, Y. Zhang, M. Rowe and M. Muhammed, *Adv. Funct. Mater.*, 2004, **14**, 1189–1196.

27 G. Tan, W. Liu, S. Wang, Y. Yan, H. Li, X. Tang and C. Uher, *J. Mater. Chem. A*, 2013, **1**, 12657.

28 H. Li, X. Su, X. Tang, Q. Zhang, C. Uher, G. J. Snyder and U. Aydemir, *J. Mater.*, 2017, **3**, 273–279.

29 L. Guo, G. Wang, K. Peng, Y. Yan, X. Tang, M. Zeng, J. Dai, G. Wang and X. Zhou, *Scr. Mater.*, 2016, **116**, 26–30.

30 E. V. Shelekhov and T. A. Sviridova, *Met. Sci. Heat Treat.*, 2000, **42**, 309–313.

31 F. Bachmann, R. Hielscher and H. Schaeben, *Ultramicroscopy*, 2011, **111**, 1720–1733.

32 C. Kittel, Ed., *Introduction to Solid State Physics*, John Wiley & Sons, Inc, 8th edn., 2005.

33 R. Franz and G. Wiedemann, *Ann. der Phys. und Chemie*, 1853, **165**, 497–531.

34 H.-S. Kim, Z. M. Gibbs, Y. Tang, H. Wang and G. J. Snyder, *APL Mater.*, 2015, **3**, 041506.

35 A. T. Burkov, A. Heinrich, P. P. Konstantinov, T. Nakama and K. Yagasaki, *Meas. Sci. Technol.*, 2001, **12**, 264–272.

36 E. Alleno, D. Bérardan, C. Byl, C. Candolfi, R. Daou, R. Decourt, E. Guilmeau, S. Hébert, J. Hejtmanek, B. Lenoir, P. Masschelein, V. Ohorodnichuk, M. Pollet, S. Populoh, D. Ravot, O. Rouleau and M. Soulier, *Rev. Sci. Instrum.*, 2015, **86**, 011301.

37 O. Guillon, J. Gonzalez-Julian, B. Dargatz, T. Kessel, G. Schierning, J. Räthel and M. Herrmann, *Adv. Eng. Mater.*, 2014, **16**, 830–849.

38 A. S. Mukasyan, A. S. Rogachev, D. O. Moskovskikh and Z. S. Yermekova, *Ceram. Int.*, 2022, **48**, 2988–2998.

39 Q. Jie, H. Wang, W. Liu, H. Wang, G. Chen and Z. Ren, *Phys. Chem. Chem. Phys.*, 2013, **15**, 6809.

40 J. I. Goldstein, D. E. Newbury, J. R. Michael, N. W. M. Ritchie, J. H. J. Scott and D. C. Joy, *Scanning Electron Microscopy and X-Ray Microanalysis*, Springer New York, New York, NY, 2018.

41 S. Ghosh, S. Meledath Valiyaveettil, G. Shankar, T. Maity, K.-H. Chen, K. Biswas, S. Suwas and R. C. Mallik, *ACS Appl. Energy Mater.*, 2020, **3**, 635–646.

42 V. I. Fistul', *Heavily Doped Semiconductors*, Springer New York, Boston, MA, 1995.

43 J. W. Sharp, E. C. Jones, R. K. Williams, P. M. Martin and B. C. Sales, *J. Appl. Phys.*, 1995, **78**, 1013–1018.

44 A. Gharleghi, P.-C. Hung, F.-H. Lin and C.-J. Liu, *ACS Appl. Mater. Interfaces*, 2016, **8**, 35123–35131.

45 A. Eucken, *Fortchg. Gebiete Ingenieurw., B3, Forschungsh.*, 1932, **16**, 353–360.

46 J. R. Drabble and H. J. Goldsmid, *Thermal Conduction in Semiconductors*, Pergamon Press, 1961.

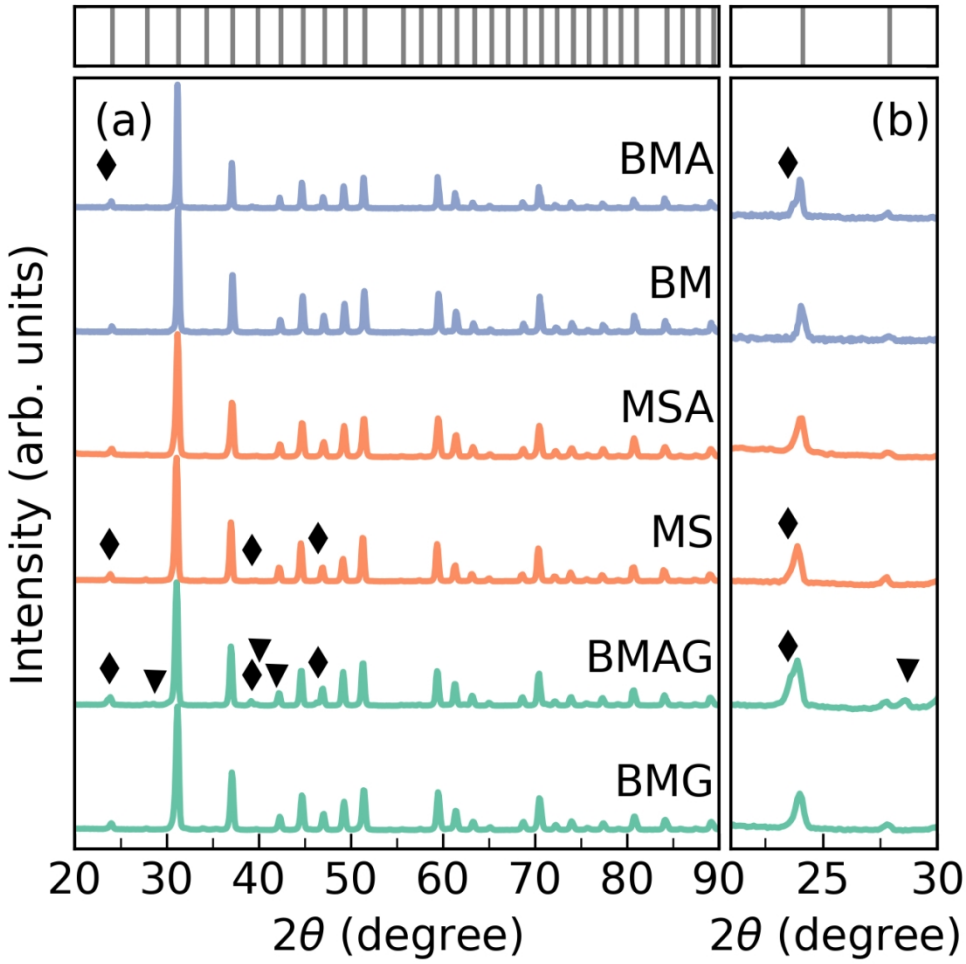

Figure 1. (a) PXRD patterns of the $In_1Co_4Sb_{12+\delta}$ samples prepared by various methods. (b) An enlarged section of (a) in a 2θ range from 21° to 30° where InSb and Sb secondary phases have the most intensive reflections. Sb and InSb secondary phases are indicated by a solid black triangle (▼) and a thin diamond (♦) symbols, respectively. Bragg's reflections for the $CoSb_3$ phase are indicated by ticks on the top part of the figure.

114x113mm (300 x 300 DPI)

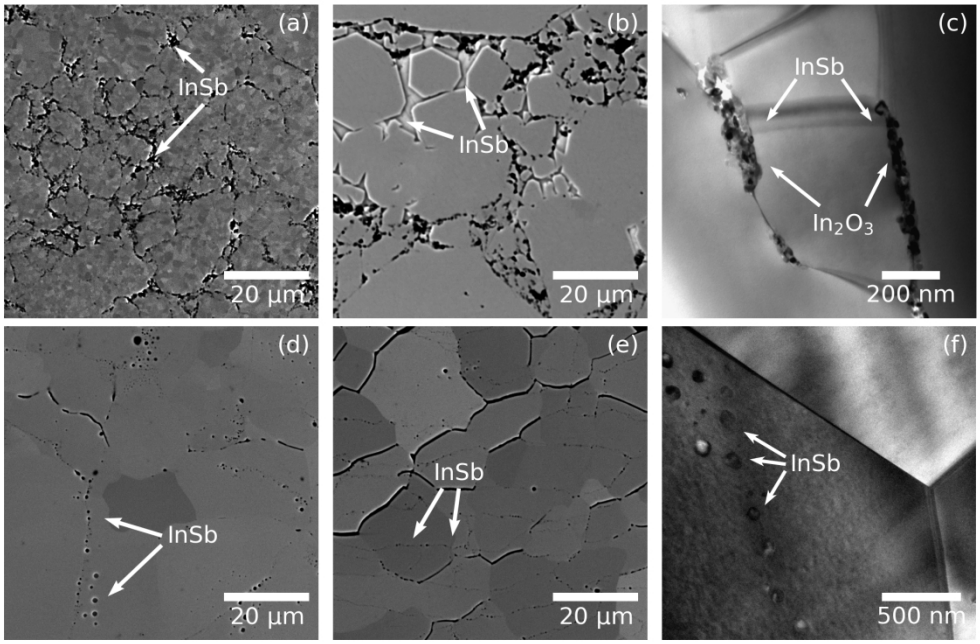

Figure 2. SEM micrographs of the polished surfaces of the (a) BMG, (b) BMAG, (d) MS, and (e) MSA bulks in electron channeling contrast mode. TEM images of the (c) BMAG and (f) MSA samples.

180x120mm (300 x 300 DPI)

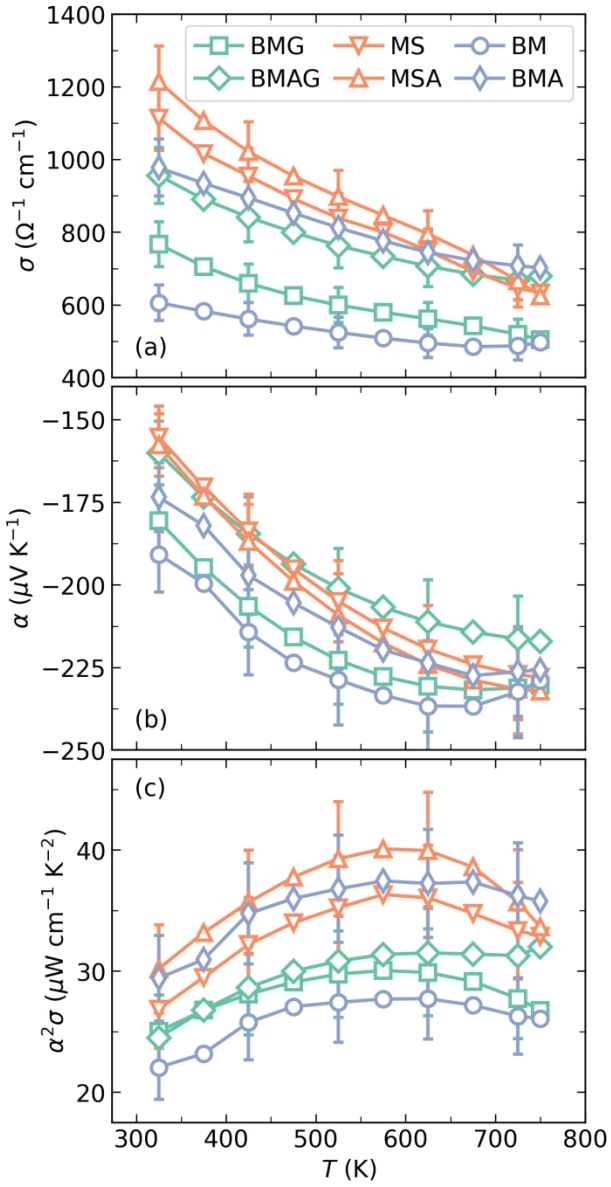

Figure 3. Temperature dependence of (a) the electrical conductivity σ, (b) the Seebeck coefficient α, and (c) the power factor $\alpha^2\sigma$ for the $In_1Co_4Sb_{12+\delta}$ samples prepared by various methods.

130x249mm (300 x 300 DPI)

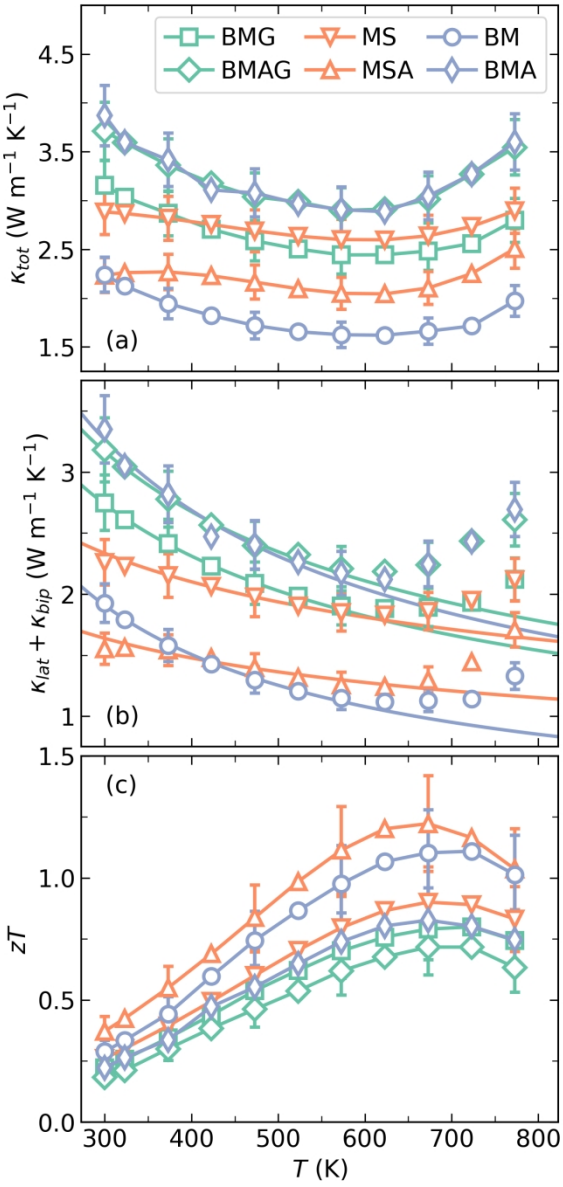

Figure 4. Temperature dependence of (a) the total thermal conductivity κ_{tot}, (b) the lattice and bipolar thermal conductivities (κ_{lat} + κ_{bip}), and (c) the figure of merit zT for the $In_1Co_4Sb_{12+\delta}$ samples prepared by various methods. Solid lines in (b) are the lattice contribution to the thermal conductivity fitted by the power law $\kappa_{lat} \propto T^{-r}$.

120x247mm (300 x 300 DPI)

Table 1. Codes, nominal and actual compositions (from the EDX analysis) normalized for 4 Co atoms, phase composition, lattice parameter *a*, crystalline size D_c (from the Rietveld refinement shown in Fig. S3), average grain size D_g (from the EBSD analysis shown in Fig. S4), and relative density *d* of the $In_1Co_4Sb_{12+\delta}$ samples prepared by various methods.

Code	Nominal composition	Actual composition	Phase composition (vol.%)	*a* (Å)	D_c (nm)	D_g (μm)	*d* (%)
BMG	$In_1Co_4Sb_{12+\delta}$	$In_{0.23}Co_4Sb_{12.39}$	100% $CoSb_3$	9.044	165 ± 50	6.0	97
BMAG		$In_{0.22}Co_4Sb_{12.35}$	94.5% $CoSb_3$, 4.3% InSb, 1.2% Sb	9.048	> 500	20.3	98
BM		$In_{0.22}Co_4Sb_{12.40}$	100% $CoSb_3$	9.050	~300	n/a	93
BMA		$In_{0.23}Co_4Sb_{12.33}$	100% $CoSb_3$ + traces of InSb	9.051	> 500	n/a	95
MS		$In_{0.29}Co_4Sb_{12.43}$	99.3% $CoSb_3$, 0.7% InSb	9.050	100 – 300	9.6	95
MSA		$In_{0.25}Co_4Sb_{12.46}$	100% $CoSb_3$	9.050	120 ± 40	10.4	93

Table 2. Codes, Hall carrier concentration, and Hall carrier mobility of the $In_1Co_4Sb_{12+\delta}$ samples prepared by various methods.

Code	n_H (10^{20} cm^{-3})	μ_H ($cm^2V^{-1}s^{-1}$)
BMG	1.29	40.9
BMAG	1.37	51.4
BM	1.13	33.6
BMA	1.49	40.9
MS	1.89	36.5
MSA	1.90	42.1